Effect of the particle size distribution on physical properties, composition, and quality of gas atomized Astroloy powders for HIP application

E. Bassini [a],*, U. Galech [c,d], T. Soria [c,d], M. Aristizabal [c,d], I. Iturriza [c,d], S. Biamino [a,b], D. Ugues [a,b]

[a] Department of Applied Science and Technology (DISAT), Politecnico di Torino, Corso Duca Degli Abruzzi, 24, 10129 Torino, Italy
[b] Consorzio Interuniversitario per la scienza e tecnologia dei Materiali (INSTM), Via G. Giusti, 9, 50121 Firenze, Italy
[c] CEIT-Basque Research and Technology Alliance (BRTA), Manuel Lardizabal 15, 20018 Donostia/San Sebastián, Spain
[d] Universidad de Navarra, Tecnun, Manuel Lardizabal 13, 20018 Donostia/San Sebastián, Spain

ARTICLE INFO

ABSTRACT

Hot Isostatic Pressing (HIP) is a well-known technique that lately is gaining more interest because of its growing involvement in the Additive and Near-Net Shape manufacturing fields. When HIP is used for near-net-shape manufacturing, the raw gas atomized powders assume the uttermost importance, and special attention should be given to their quality and characteristics. Based on this statement, the powder should be sieved directly after production to select only those that best suit the HIP process. Typically, a broad Particle Size Distribution is indicated for HIP purposes and looks economically advisable because it leads to a higher yield. Despite this, if the PSD is not strictly controlled, particles with high Oxygen content or chemical inhomogeneity could enter the production chain, leading to compacted components with insufficient mechanical properties. In this paper, Nickel-based superalloy Astroloy particles were assessed in depth both at their surface and in the core, dividing them into sub-batches via mechanical sieving. This procedure evidenced which contribution was brought to the final raw material by each sub-batch. Furthermore, physical properties such as flowability and tap density were studied as a function of the PSD. Next, a complete morphological assessment was conducted to understand the possible defects of each sub-batch better. Similarly, every particle group was chemically studied to determine the Oxygen, Carbon, Nitrogen, and Hydrogen content of each sub-batch. Micro and nano indentations combined with EBSD were used to understand how the particle size may affect the mechanical properties of the powders during the Hot Isostatic pressing. Furthermore, EDS and XRD analysis were used to thoroughly understand how Ti segregation starts forming and what effects are likely to develop. Based on these investigations, it was possible to rationally identify the upper and lower boundary for particle PSD without excessively limiting the overall process yield.

© 2021 Elsevier B.V. All rights reserved.

1. Introduction

Nowadays, more and more manufacturers involved in the production of components in the aeronautical, energy production, and oil and pump fields started using the Hot Isostatic Pressing (HIP) of gas-atomized powders for parts manufacturing. Such a technique is convenient to produce steel or nickel-based superalloys components of simple and complex shapes. Applications are found in steam turbines, aeronautical engines, offshore sub-sea, and tool manufacture [1].

There are several advantages of this manufacturing method concerning the traditional ones. For instance, the HIP components show a higher degree of cleanliness and a more homogeneous microstructure. Moreover, HIP allows a near-net or net-shape approach, leading to low machining cost and buy-to-fly ratios. Hot Isostatic Processing gives homogeneous and isotropic mechanical properties even when a material with low castability or forgeability is involved because segregation is wholly avoided.

The final component is obtained by filling a pre-shaped steel capsule made from TIG welded mild steel plates with powders onto a vibrating surface. The consolidation is obtained with a tailored procedure that strongly depends on material nature. For example, Raisson, in his published works [2,3], describes how to get full-dense

* Corresponding author.
 E-mail address: emilio.bassini@polito.it (E. Bassini).

Table 1

Chemical composition of Astroloy powders.

Element	Ni	Co	Cr	Mo	Al	Ti	Fe	Zr
w%	Bal.	16.7	15.3	4.9	3.8	3.6	0.05	0.0001

Table 3

Levels of oxygen, nitrogen, and hydrogen measured in the un-sieved particle batch.

O [ppm]	N [ppm]	H [ppm]
115 ± 12	127 ± 7	5.4 ± 3

Astroloy components from powders by heating above the γ' solvus temperature, i.e., at 1160 °C. At the same time, in his review, Hjorth reports how HIP could be used to successfully produce fittings, valve components, manifolds, swivel parts, diesel engine nozzles, turbine parts, centrifugal separators, and components for medical purposes [4].

Today most of the Hot Isostatic Presses rely on natural cooling systems which generate slow cooling rates (1–5 °C/min). Notoriously, nickel-based superalloys containing γ' suffer from low cooling rates and should be cooled at a considerably higher speed. The higher the cooling rate, the smaller the reinforcing precipitates and the better mechanical properties. However, typically HIP provides a slow cooling rate, leading to superalloys with coarse γ' (especially those located at the grain boundaries), showing inferior mechanical properties. This issue can be solved by performing a complete heat treatment as the ones proposed by Bassini et al. in their previous works [5,6].

Finally, the manufactured components are leached to remove the plain steel capsule and then properly machined to remove the outermost altered layer, as observed in this research group's previous work [7].

However, the final result is strongly related to the quality of the raw material, i.e., the atomized powder, which must be utterly free from non-metallic inclusions and foreign metallic particles. Moreover, the gas-atomization process itself plays a vital role in determining the powder quality. Oxygen content is one of the most important factors to monitor in powders because its content directly affects the precipitation of carbides on Prior Particle Boundaries (PPB) after solidification has occurred. PPBs typically act as crack initiation sites which lower the mechanical properties, especially ductility [8–10]. Moreover, the PPB networks are practically impossible to be eliminated after their precipitation.

Although some authors, like Chang et al. [11], were able to process IN718 samples free of PPBs, using a tailored HIPping cycle consisting of two temperature densification process, researchers are still concerned by PPB networks.

According to literature, Ti and Zr can react with the oxygen bond at the surface of the particles, and there, very stable oxides are likely to form. These oxides are then responsible for the formation of the PPBs. Thus, in other words, it can be stated that an excess of adsorbed Oxygen will directly affect the PPBs precipitation [11,12].

For example, Liu [11] HIPped oxidized particles obtained by heating them at 500 °C and compared the results with consolidated parts obtained from as-received powders. His experimental work demonstrated that PPBs fraction was significantly higher when powders were oxidized. Another critical factor to address is that powder oxygen content strongly depends on particle size. Rao studied the oxygen content of inert gas atomized powders of IN718 and noticed how the size of the particles influenced the oxygen content. More specifically, the smaller the particle size, the higher the oxygen content detected. Furthermore, HIPped samples containing higher

oxygen content show a higher fraction of PPBs where Ti and Nb MC carbides were formed [12]. Basically, according to these experiments, batches containing small particles should be discouraged to reduce the side effects mentioned above.

Despite this, using a batch of powders with a wide range of particles (i.e., containing smaller and larger particles together) is appealing for two main reasons: it allows to increase the tap density of the powders, which is helpful during the densification process, and it helps to reduce material waste during the atomization, increasing its overall yield. Nonetheless, smaller powders are more prone to adsorb Oxygen due to their larger specific area, while very large particles suffer from inner porosity and elemental segregations. This paper aims to find the best compromise between atomization yield and powder quality by analyzing different powder batches with other particle size distributions. For this purpose, the Astroloy Powder batch was sieved in different sub-groups to assess each powder category contribution separately. The morphology and the content of interstitial elements were evaluated for each subgroup of powders, and a suggested low and high size-cut is finally provided.

2. Methods

2.1. As-received powder batch

In this work, a batch of commercial Astroloy powder was analyzed in depth.

The chemical composition of the powders was determined via ICP-OES (Inductively Coupled Plasma-Optical Emission Spectroscopy) using a Varian 725-ES and is reported in Table 1. Conversely, Table 2 contains all the principal physical properties for the un-sieved batch of particles.

Astroloy non-interstitials elements were.

Table 2 shows the most important physical parameters of the powders as a function of the powder side distribution (PSD); As reported in the table, by sieving the particles, their flowability and tap density present significant differences. When the test is performed on un-sieved powders, the measurement of the flowrate fails, being impossible to pass through the Hall and Carney funnel. This effect is connected to the presence of fine particles ranging between 10 and 63 μm, due to their high cohesion energy [13,14]. As shown in Table 2, this particle category is unable to flow by itself and hinders the flowability of a broader batch in which these are contained. Conversely, particle behavior drastically changes as soon as this specific sub-batch is removed. In other words, to strongly enhance the powder flowability of Astroloy powders, their finer fraction should be sieved away. By doing so, the capsule filling procedure would become more accessible and faster [15]. On the other hand, this decision would bring two main side effects: 1) a lower yield of the IGA and a severe amount of particle waste; 2) a lower Tap density which could result in higher porosity levels in the final
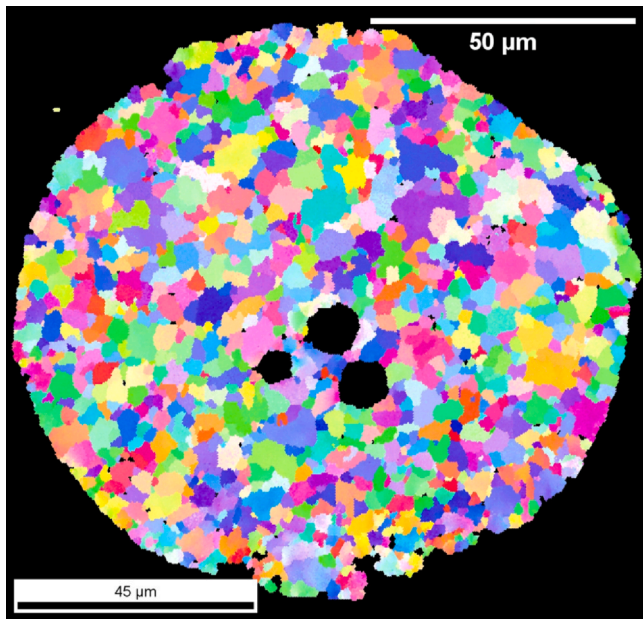
Table 2

Main physical properties measured for an un-sieved batch of powders.

Batch PSD [μm]	Flow rate (s/50 g)	Apparent density (g/cm^3)	Tap density (g/cm^3)	Pycnometer density (g/cm^3)	Tap density (%)	Theoretical density (g/cm^3)
10–150	No Flow	4.490 ± 0.020	5.195 ± 0.002	7.867 ± 0.001	65.10	7.98[a]
10–63	No Flow	4.390 ± 0.030	5.172 ± 0.001	7.882 ± 0.003	64.82	
63–100	17.03 ± 0.07	4.562 ± 0.006	5.000 ± 0.001	7.791 ± 0.002	62.66	
100–150	26.34 ± 0.02	4.031 ± 0.006	4.461 ± 0.001	7.463 ± 0.003	55.90	

[a] Based on the density of an as-HIP sample, obtained with 10–150 μm ranging powders).

Fig. 1. EBSD map of a particle of 114 μm showing the axis selected.

compact after Hot Isostatic Pressing. Together with the following experimental results, these facts should be carefully assessed to maximize the system's yield without incurring further limitations during the HIP process [16].

Finally, the un-sieved batch powder size distribution shows a d10, d50, and d90 of 14.7, 35.5, and 96.4 μm, respectively. The smallest and largest particles had a diameter of 2.4 and 211 μm, respectively.

2.2. Preparation of powder sub-batches

The chemical and morphological properties of the powders were assessed by dividing them into different classes, hereinafter called sub-batches. First, the entire batch was sieved using standard mesh, whose numbers are: 140, 200, 230, 270, 325, and 400, respectively. More precisely, to mechanically sieving the powders, the particles were heated in a vacuum furnace at 135 °C for 2 h. Then, the dried powders were transported to the sieving rig in a glass desiccator to reduce moisture contaminations. The use of 300 g of Astroloy

powders was considered sufficient to get enough powder for each sub-batch. Finally, all the powders were sieved under vibration in three different steps for half an hour, processing only 50 g of material per time not to clog the mesh.

2.3. Interstitial element assessment

The assessment of Carbon and Sulfur was obtained with a Leco CS 744 after sample combustion. Five samples of un-sieved particles weighing 1 g each were measured, and the average Carbon and Sulfur content were 178 ± 4 ppm and 18 ± 1 ppm, respectively. The sampling was repeated later on the sub-batches obtained according to the previously described procedure. In this case, three samples per class were examined.

O, N and H were measured using a LECO ONH 836 via melting under inert gas using He as the carrier media. This analysis was performed using the same test scheme described for C and S assessment; all the samples weighed 1 g. As previously done, also these elements were assessed without sieving the powders, and the average values are shown in Table 3.

2.4. Morphological assessment of the powders

After the physical and chemical assessment, powders were prepared for the morphological observation using an electronic scanning microscope Zeiss EVO 15 using both secondary and backscattered electron detectors. Powders were observed in the top view and in the cross-section. Astroloy powders from each sub-batch were deposited on SEM stubs for top view observation. On the other hand, for cross-sections, powders were embedded in phenolic resins and ground with sic papers. Only 600 and 1200 grits were used. Polishing was obtained with diamond pastes of 3 and 1 μm, and final finishing was obtained through colloidal Silica. The powders' dendritic and cellular microstructure was already visible in as-polished condition. Despite this, to better appreciate the size of the secondary dendrite arm spacing, Kalling n.2 (waterless) was used as etching media. The EDS analysis was carried out with an Oxford instrument probe Ultim Max equipped with a 170 mm^2 Silicon Drift Detector.

2.5. XRD analysis

XRD analysis was carried out by using an X-Pert Philips diffractometer using copper as the cathode. The instrument was used in a Bragg Brentano configuration applying 40 kV and 40 mA with a step size of 0.013°. The detector had a holding time per each step of
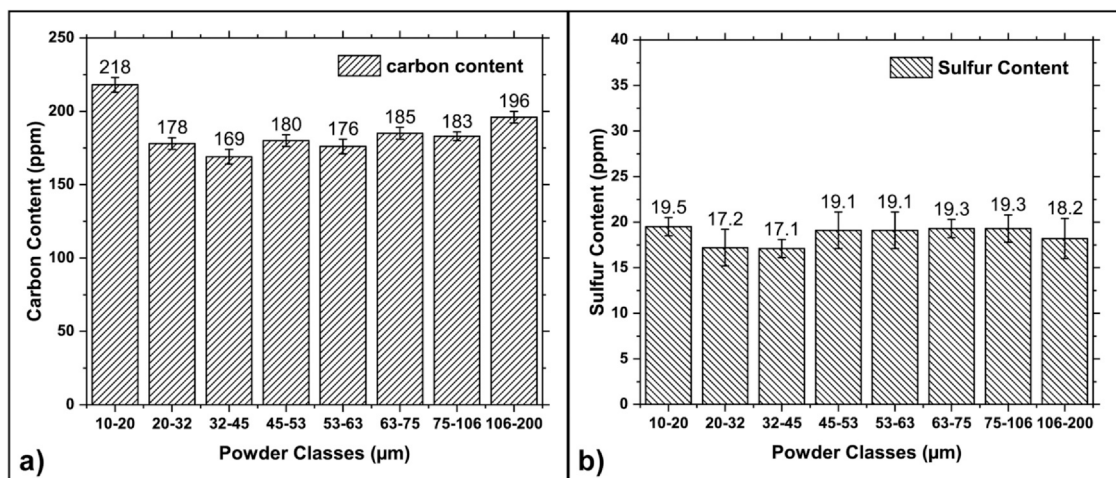

Fig. 2. Carbon (a) and Sulfur (b) content measured in the different powders sub-batches.
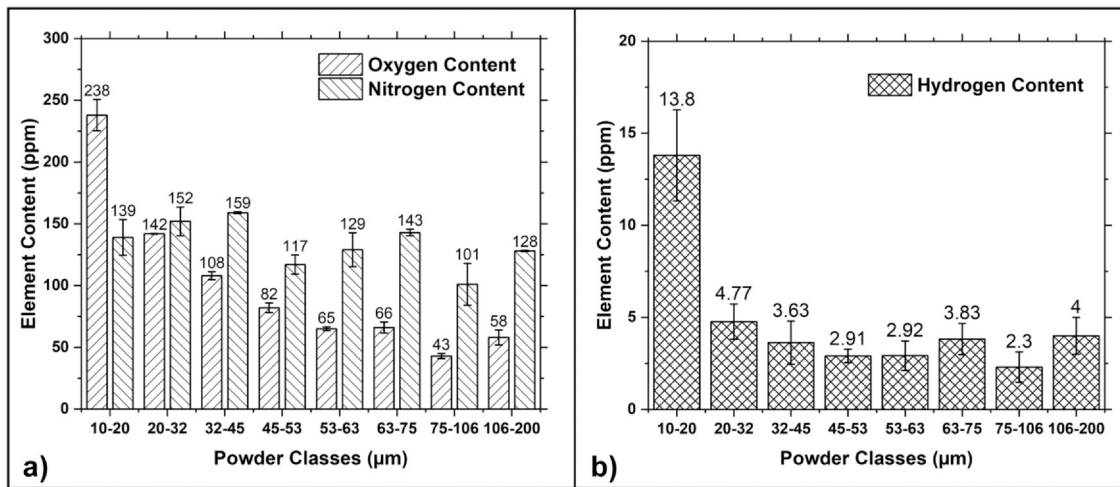
Fig. 3. Oxygen and Nitrogen (a) and hydrogen (b) content, measured in the different powder sub-batches.

35 s. In particular, the XRD diffractogram was recorded in the 20–100° 2Θ range.

2.6. Micro Vickers hardness assessment

Microhardness measurements were performed on each particle sub-batch in the cross-section, except for those smaller than 20 μm, which could not be assessed due to insufficient thickness. Ten indentations were taken per class, applying 15 g. All the indentations were sufficiently small to be entirely contained within the powders cross-section. The test was performed with a Leica VMHT. The imprint diagonals were measured with image analysis software to reduce the total uncertainty.

2.7. Nano hardness assessment

Nanohardness measurements were carried out in a powder particle with a diameter of 123 μm; this was polished up to colloidal Silica. A matrix of 5 × 5 nanoindentations was conducted using a Berkovich diamond tip up to a maximum penetration depth of 200 nm at a rate of 14 nm/s. The test was completed with a TriboIndenter™ equipment. This equipment has an x-y positioning precision below 0.5 μm, which allows indenting the particle with the accuracy needed. The hardness was obtained from force vs. displacement curves using the method proposed by Oliver and Pharr [17]. The particle size was measured with image analysis software to be as accurate as possible. Furthermore, the studied particle was analyzed in the cross-section with an electronic microscope ZEISS

SIGMA 500 FEG-SEM using secondary and backscatter electron detectors.

2.8. Grain size analysis

EBSD measurements were performed on a Philips XL30cp SEM using TSL (TexSEM Laboratories) MSC 2200 equipment and the post-processing in TSL-OIM® for every sub-batch of powders. Samples were mounted in a conductive resin and polished up to colloidal Silica. A step size of 0.3 μm was chosen to reveal even the smallest grains. The scan area was tuned, so the number of grains was as high as possible to reach a considerable number of grains per range. To obtain significant statistics, grain size values (above 300 grains per range), 16 particles from 10 to 20 μm range, and 4–7 particles from the rest of the batches were analyzed. The data obtained were post-processed using a 10° grain tolerance angle and a minimum grain size of 3 pixels.

The particle sizes were determined, taking into account the longest axis and its perpendicular, obtaining the average diameter, as shown in Fig. 1.

3. Results

3.1. C, S, O, N, and H content as a function of particles size

Fig. 2 shows the Carbon and Sulfur content measured in each powder sub-batch. The powder size slightly alters the Carbon content. More specifically, its content is higher in the finest and largest particles, respectively. The minimum C content was found in the
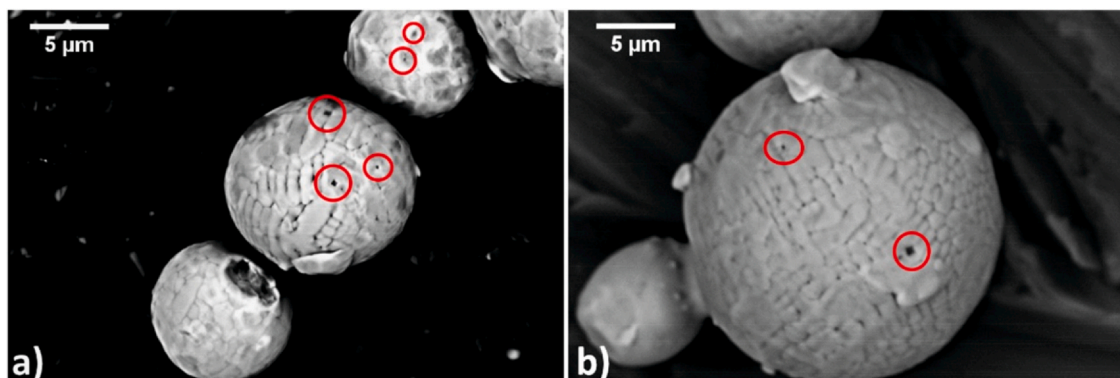

Fig. 4. Top view of particles with the diameter ranging between 10 and 20 (a) and between 20 and 32 (b).
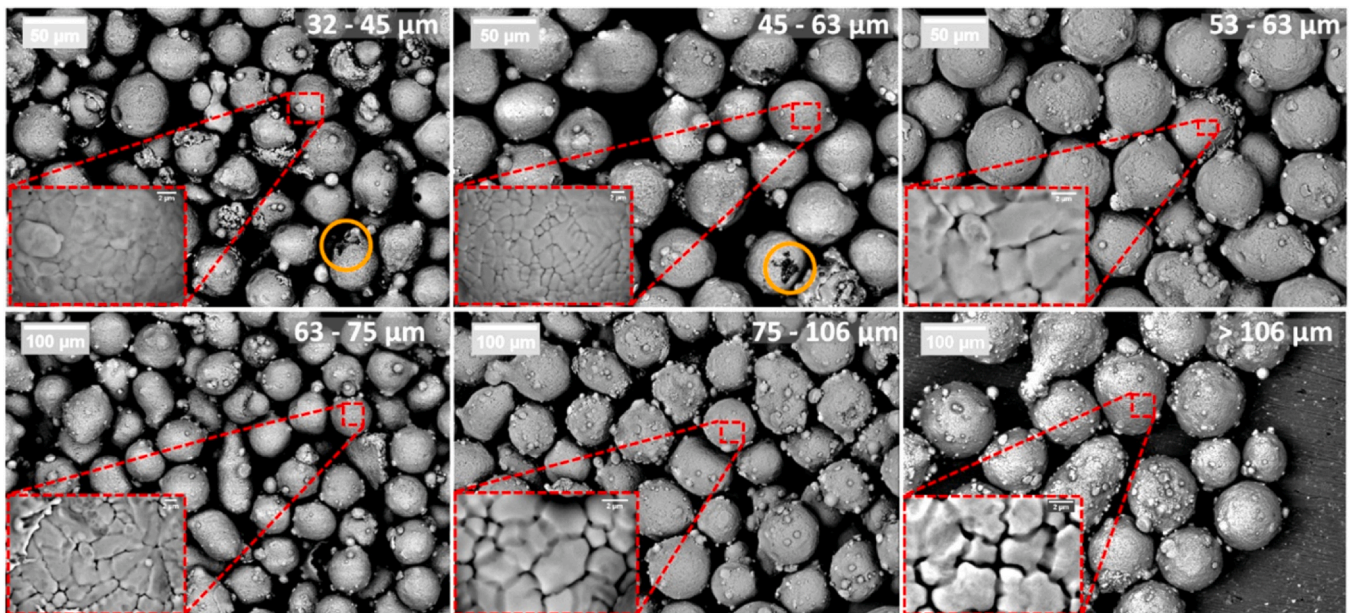
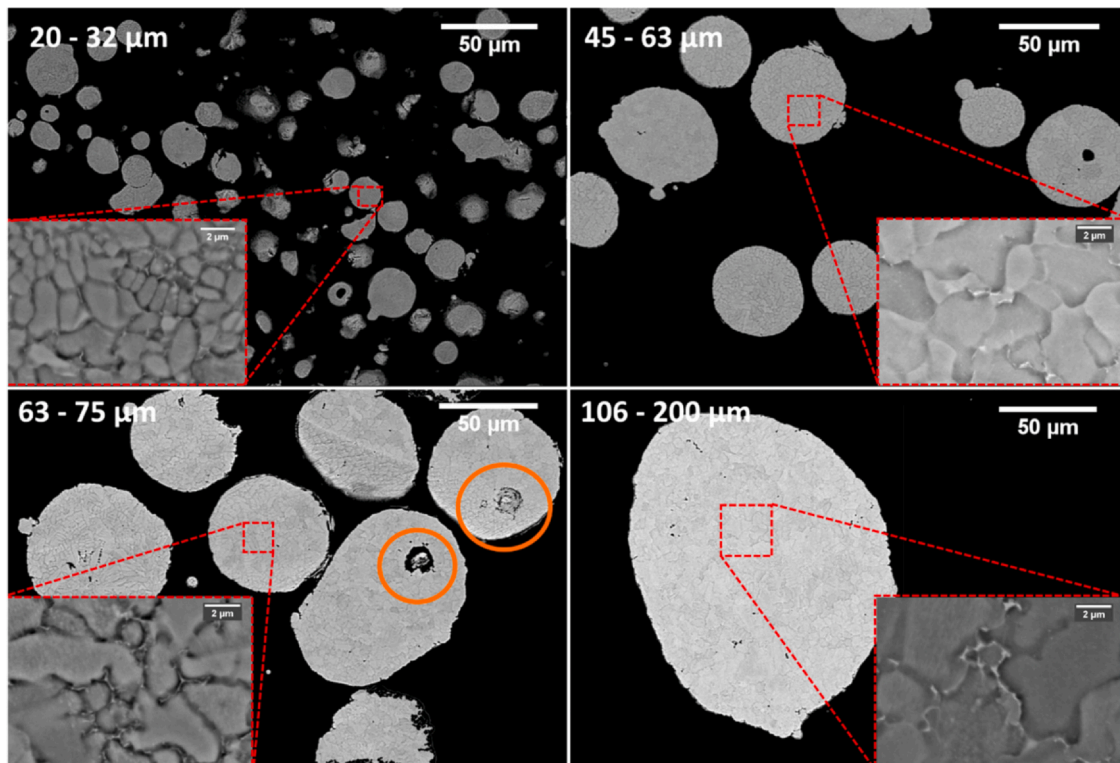**Fig. 5.** Top view of particles with the diameter ranging between 32 and 45 (a) 45–63 (b) and 53–63 (c).

Fig. 6. Powders in cross-section of the following sub-batches 20–32 µm (a)45–63 µm (b) 63–75 µm (c) and 106–200 µm (d).

32–45 µm sub-batch. On the other hand, Sulfur is unaffected by the powder size.

Fig. 3 shows how the particle size affects the interstitial element content. More specifically, Oxygen content clearly shows a decreasing trend as the powders get coarser. On the other hand, nitrogen content, similarly to Sulfur, seems unaffected by the particle size. Finally, H content is higher only for powders below 20 µm. This trend can be probably explained considering that finest particles have a higher tendency to form a thin $Ni(OH)_2$ layer due to their more elevated specific surface [18,19].

3.2. Powders in top view

Generally speaking, Inert Gas Atomized Powders are primarily spherical. Some of the typical defects are small or large satellites adhered to the powders or films known as cold splat. Fig. 4a) shows particles with a diameter ranging between 10 and 20 µm, while Fig. 4b) shows particles with a diameter ranging between 20 and 32 µm respectively. These particles clearly show a dendritic structure. The smallest particles do not show any satellite, unlike the bigger particles where the presence of some satellites is noticeable. Large and
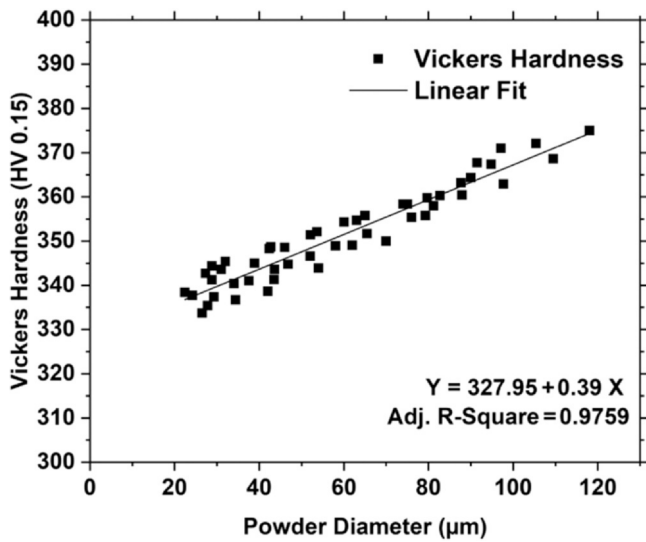
Fig. 7. Particles hardness as a function of their diameter.
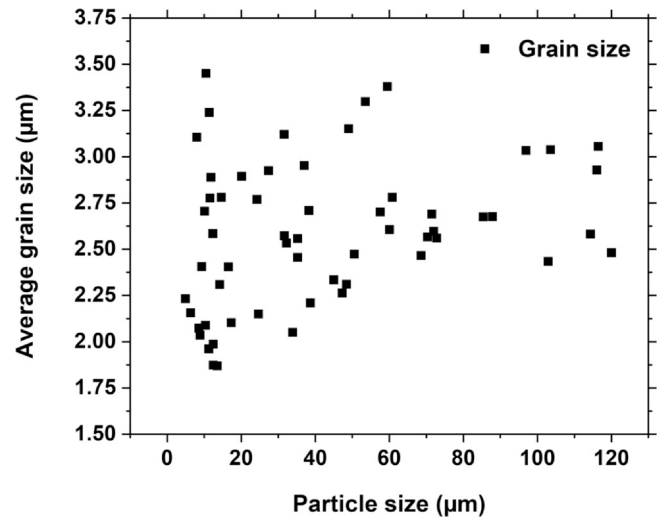

Fig. 9. Grain size as a function of particle size, EBSD measurements.

small particles show several Titanium carbides, easily identifiable because of their squared shape and black color [20]. Some of them are highlighted using a red circle. It is noteworthy that the smaller the particles, the higher is the observable carbide density.

Fig. 5 shows all the other powder sub-batches in the top-view; each picture also has an insert in which the interdendritic region is evidenced. These particles are primarily spherical, although some of them have a very irregular shape. The most visible defect is numerous and small satellites that are rarely larger than ten μm.

Furthermore, TiC carbides were not evidenced anymore. Finally, only a tiny fraction of powders showed open porosity, as evidenced by an orange circle below. Subsequently, the bottom part of Fig. 5 shows the larger particles. More specifically, those particles ranging between 63 and 75, 75–106, and 106–200 μm, respectively. These particles, with some exceptions, are also spherical despite the larger ones show more accentuated shape irregularities. For what concerns the largest particles sub batch (i.e., those which range between 106 and 200 μm), some elliptical particles were observed, which could
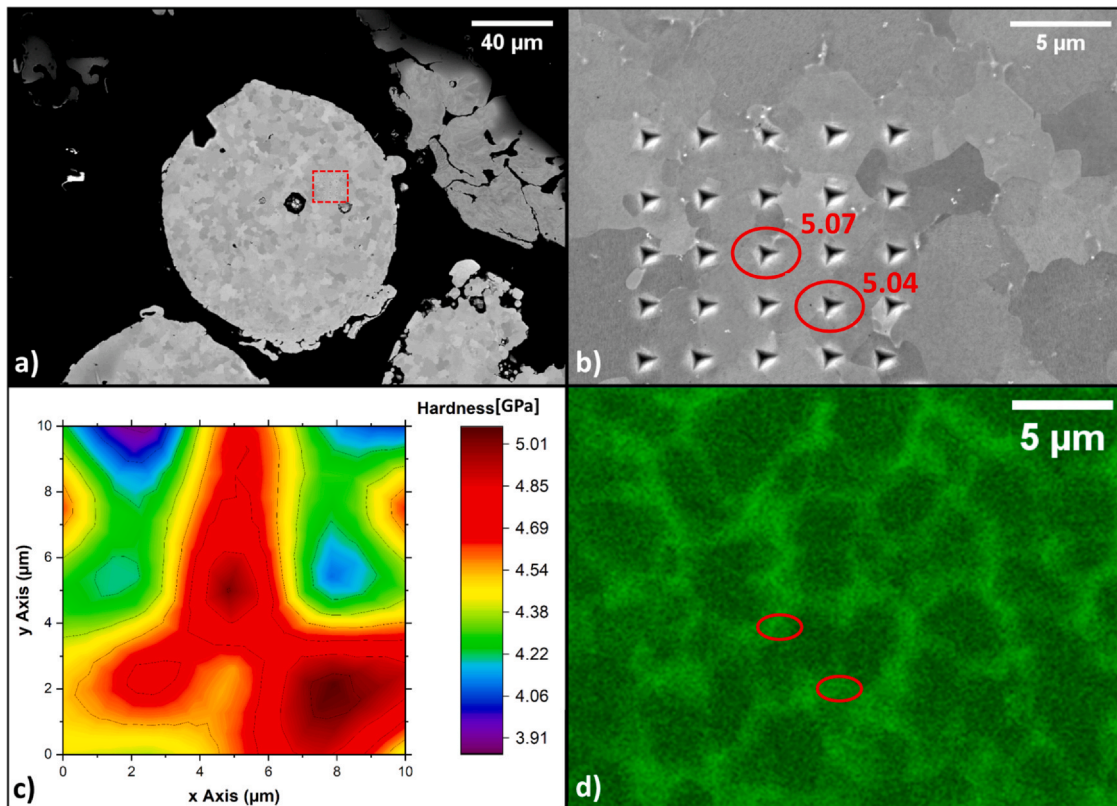

Fig. 8. Nano indented particle (a) a zoom of nanoindentation matrix area. Values from Ti segregation areas were indicated in red (b) the complete contour map with all the hardness values assessed (c) and EDS map showing the position of two indentations onto a Ti segregation (d).
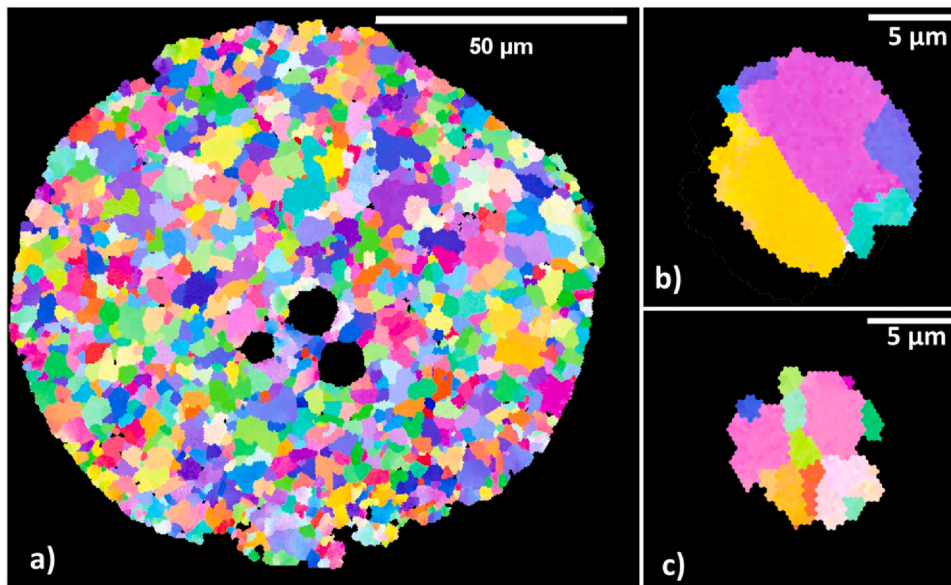
Fig. 10. EBSD maps of particles, large (114 μm) (a) small (12 and 9 μm) (b).

have formed during cooling from melting due to the joining of two independent spheres. Fig. 5 shows the satellite density increasing as the particle size increases.

3.3. Powders in cross-section

The analysis of the powder cross-section is a helpful tool to assess the average dendritic spacing and the actual presence of segregation at the interdendritic arms. The sub-batches mentioned above were embedded in resin and then grounded and polished. The resulting microstructures and defects are described below.

Fig. 6 shows four powder sub-batches, i.e., the samples with powder in the following ranges: 20–32, 45–63 63–75, and 106–200 μm. The development of the dendritic microstructure is strongly related to the particles' cooling rate, which, in turn, is connected to the particle's size. More specifically, the larger the particles, the slower the cooling rate. Consequently, below a critical cooling rate, segregation may happen, as demonstrated in the inserts contained in the following pictures. As a result, all the samples show a fully-developed dendritic microstructure. Segregations in the interdendritic region, on the other hand, are progressively more visible in coarser particles.

As the particles get coarser, larger dendrites can be observed, as demonstrated later by assessing the secondary dendrite arm spacing.

A further noticeable difference is the shape of the pores, which changes between fine and coarse particles. Fine powders only show small and spherical pores, while larger particles have pores with a more complex shape similar to shrinkage porosity observable in casting components. Furthermore, in some cases, during the atomization, some liquid may trap smaller powders already solidified. The result is that the smallest particles are wrapped within a larger one, as in the case reported in Fig. 6 with orange circles. The interface between the particles is always evident and depending from case to case, this can be continuous or fragmented. In some cases, the polishing process may extract the inner particle leaving an extensive porosity.

3.4. Vickers hardness

Fig. 7 is gathering the hardness measurements obtained on the cross-section of powders with different sizes. As can be observed, there is a linear relationship between the particle size and hardness, indicating that larger particles will be harder and, thus, characterized by higher yield stress. Experimental results were linearly interpolated, and the resulting equation and adjusted R^2 are shown as well. This outcome has to be considered, especially during the HIP process, since the largest particles may be more difficult to be deformed under isostatic stress, despite the high temperature used within the furnace.
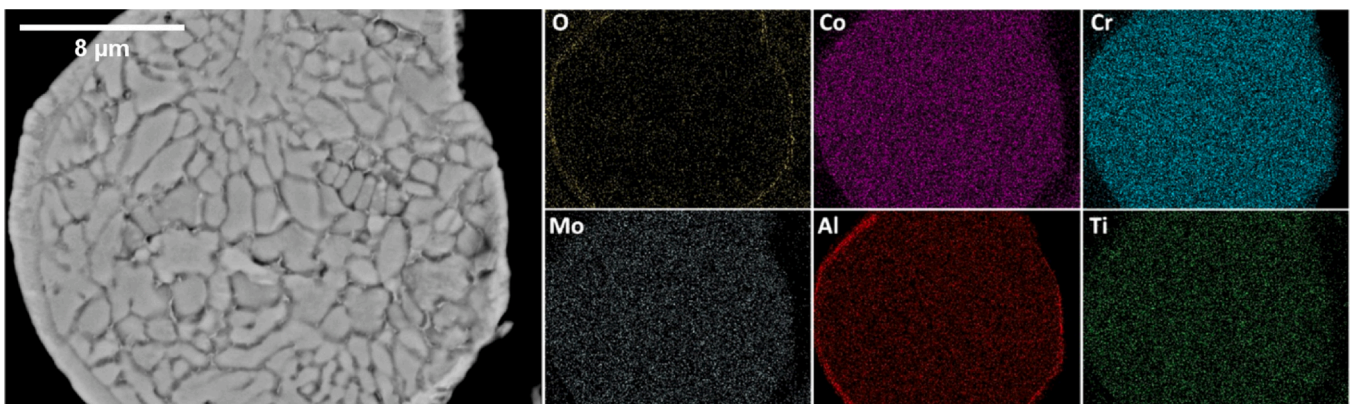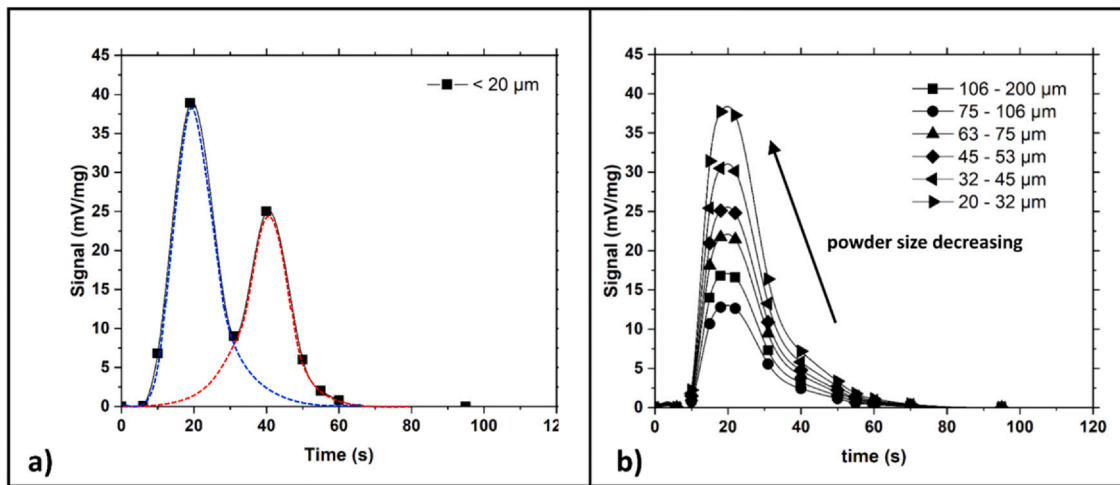

Fig. 11. EDS maps for particles with a diameter of 24 μm. The panel on the left shows the electron image, while colored pictures show how elements (O, Co, Cr, Mo, Al, and Ti) are distributed within the particles.

Fig. 12. Oxygen emitted during melting in Leco test; powders with the smallest diameter show a double peak (a) all the other particles present a single peak with different amplitude, depending on the average powder size.

3.5. Nano hardness

A nano-hardness matrix with 25 indentations performed in a powder particle is shown in Fig. 8a–c. Furthermore, Fig. 8(d) shows zones where the amount of Titanium is higher in a brighter green. It was observed that the nano-hardness values were higher, around 5 GPa, in the areas with an intense amount of Ti segregation, Fig. 8(b, d). On the other hand, the nano-hardness of intergranular sites without Ti segregation show smaller values, around 4 GPa.

3.6. Grain size analysis

Fig. 9 shows the grain size as a function of the powder particle size. Again, the results indicate that there is not any clear relationship between the grain size and the particle size.

The grain size exhibits a considerable scatter with values from 2 μm up to 3.5 μm. Considering that the number of grains is higher in bigger particles than in smaller ones, it is comprehensible that the scatter is even higher in the small particles, as demonstrated in Fig. 10.

4. Discussion

4.1. The oxide layer of particles with a diameter smaller than 20 μm

The analysis of the particles smaller than 20 μm revealed that some carbides are already formed on their surface. Moreover, an oxide layer was either evidenced by performing more in-depth analysis on powders in cross-section, as described below.

The outer layer of the cross-section of thinner particles has been analyzed. From a morphological perspective, the outer shell is different from the particle's inner part, which shows a dendritic microstructure. Therefore, the use of the EDS maps was essential to identify the nature of the oxide, which was rich in Al, as shown on the right side of Fig. 11.

The formation of an aluminum oxide layer can be explained by considering the Ellingham diagram for oxide stability. Aluminum is located right below Titanium, so Aluminum will be the first to react with atmospheric oxygen. The aluminum oxide shell act as a passivating layer that hinders any other oxidation reaction, thus preventing Titanium from being extracted toward the surface. For this reason, Titanium remains primarily located in the interdendritic regions as a consequence of elemental segregation. Furthermore, the Al atomic radius is slightly shorter than Titanium one; thus, its diffusivity will be facilitated. Similar theories were also proposed by Kuo and Kakehi [21], who worked with a different nickel-based superalloy containing Cr Ti and Al as in the current work.

The presence of an oxide layer on the smallest particles can be further confirmed by comparing the results obtained during the assessment of the oxygen content of the particles.

Fig. 12(a, b) show the generation of Oxygen under melting as a function of time during its assessment. The left panel shows the results for powders with a diameter below 20 μm, while the right
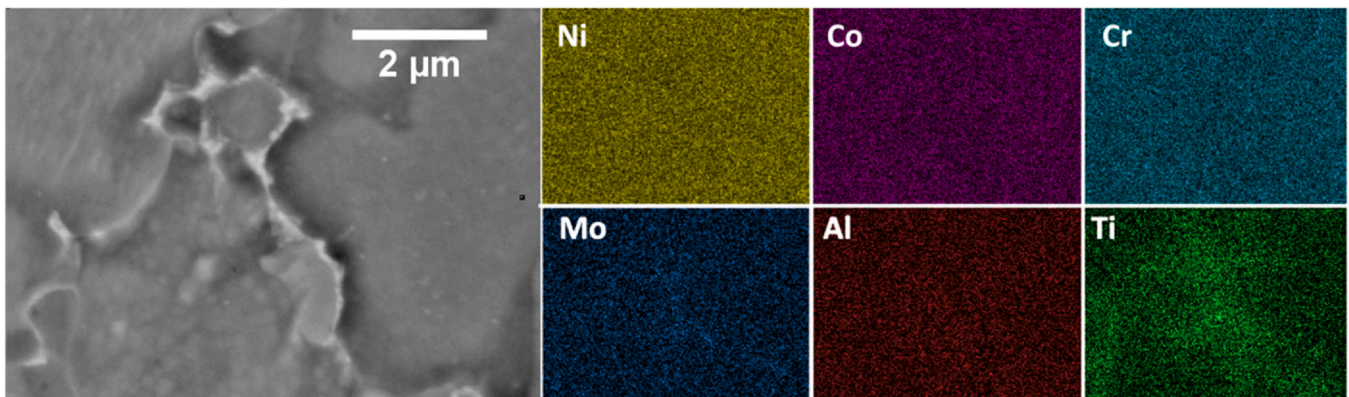
Fig. 13. EDS maps for particles with a diameter of 128 μm. The panel on the left shows the electron image, while colored pictures show how elements (Ni, Co, Cr, Mo, Al, and Ti) are distributed within the particles.
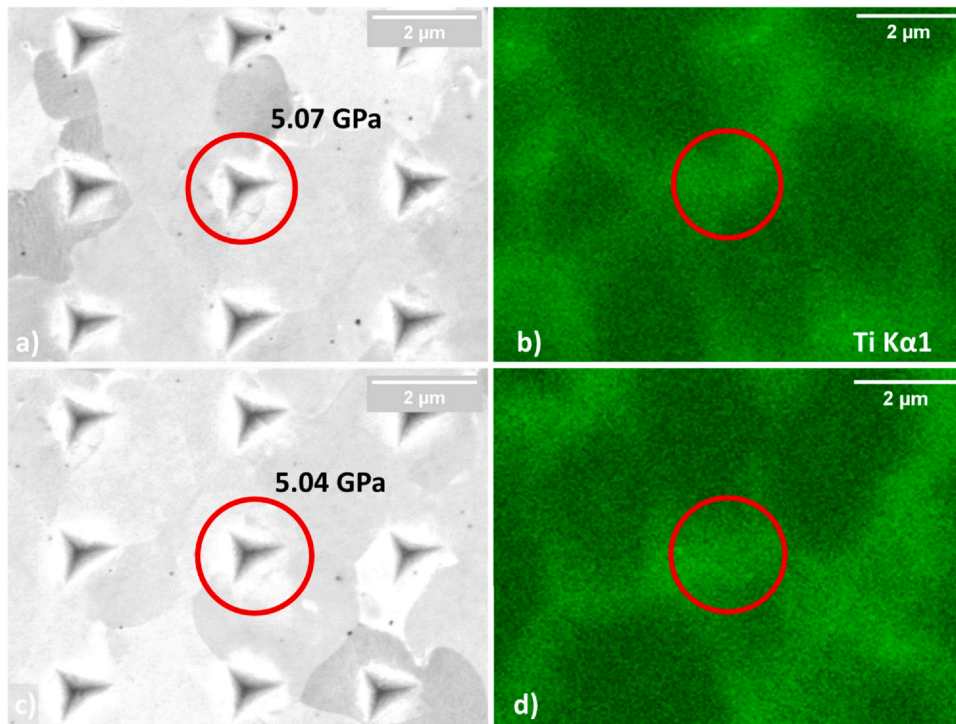
Fig. 14. Nanoindentation of the highest value (5.07 GPa) (a) and its Ti segregation map (b).
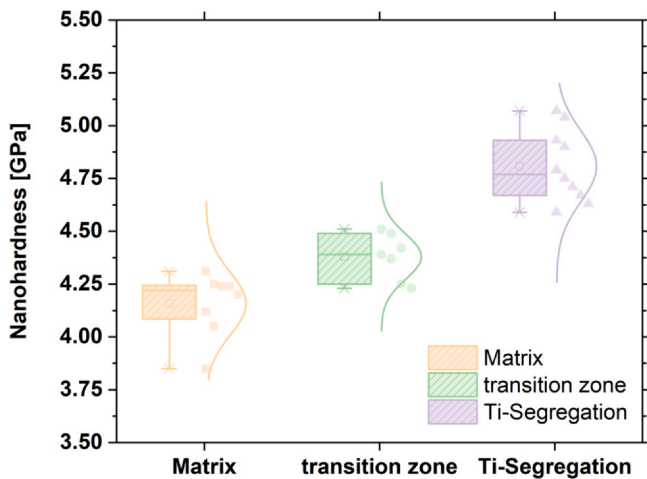

Fig. 15. Nanoindentation values divided by their location. Ti segregation areas in purple, matrix-Ti segregation areas in green, and matrix in orange.

Fig. 16. Linear relationship between particles diameter and secondary dendritic arm spacing (SDAS).

one those for all the other particle families. As can be seen, the smallest particles reveal two separate peaks while all the other particles show just one.

The assessment of interstitial elements (O, N, and H) is performed by melting the sample at a fixed temperature in a graphite crucible. The presence of a double peak may be explained as follows. Oxygen in the powder is emitted in two separate steps: From the molten metal (which has a lower melting temperature) and the aluminum-rich layer. For this reason, the peaks were fitted to a gaussian curve and integrated. The entire area underlying the peaks was calculated, and it was noticed that the first one accounts for 60.1% while the second one for 39.9%, respectively. Although the second peak is generated by a compound extremely rich in O, the oxide layer is very thin. Therefore, it occupies only a small volume, explaining why the second peak is so smaller. All the curves obtained for larger particles were subj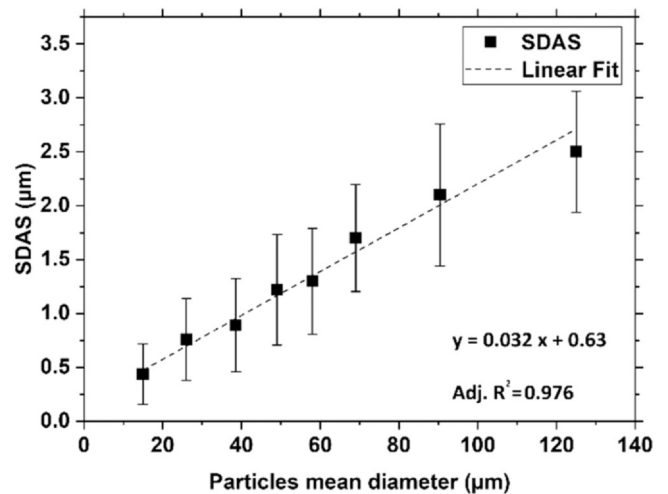ected to a deconvolution process. As a result, secondary peaks were constantly observed, having their maximum between 40 and 45 s, as in powders smaller than 20 μm. Nevertheless, the integration of these peaks leads to minimal contributions, so small that they can be neglected. The reason for such a sharp transition may be related to two principal facts. Firstly, as the particle became larger, the specific surface area decreases, limiting the contribution of the superficial oxide layer to the formation of a clear secondary peak. Secondly, the particles smaller than 20 μm haven't any lower sieving limitation; thus, this particle category also contains elements measuring just a few micrometers. Such particles will strongly contribute to the definition of a net secondary peak, as shown in the left panel of the picture below.

As discussed above, the presence of an oxide layer appears as a concern in all those powder metallurgy techniques that densify metal through high pressure and temperature, as for HIP. The
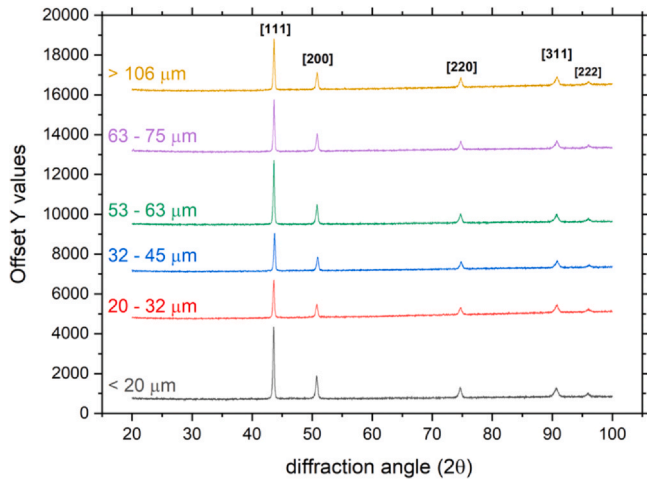
Fig. 17. Diffractograms for sieved Astroloy powders. The only differences were noticed in the peak width remove the s from angles.

principal reason is that these layers cannot be dissolved at normal HIP temperature and are likely to cause PPB formation, as described by many authors in the introduction.

4.2. The Ti segregation in oversized particles

The analysis performed on the powders cross-section evidenced that as the particle size increases, the cooling rate during solidification decreases. This condition leads to stronger Titanium segregation in the interdendritic regions of the powders. On the other hand, all the other elements such as Cr, Co, Mo do not suffer from this phenomenon. For example, Fig. 13 shows a particle of 128 μm, which presents a Ti segregation in the interdendritic region. At the same time, the other elements are evenly distributed.

Regions with Ti segregation are easily identifiable in the electron images because they appear brighter and fibrous. However, the extent of these areas decreases as the particles become smaller and cannot be any longer identified using EDS when they range between 45 and 52 μm. In other words, it exists a threshold size and thus a critical cooling rate below which Ti segregation may occur [22]. For these reasons, the dendritic microstructure of the powders was studied, and the respective secondary dendrite arms spacing was calculated, aiming to identify the actual cooling rate of each powder category. After this investigation, a critical cooling rate for avoiding Ti segregation was evidenced, as described in the next section.

Furthermore, nanoindentations in a relatively large particle, where Ti segregations were evident, revealed higher hardness values
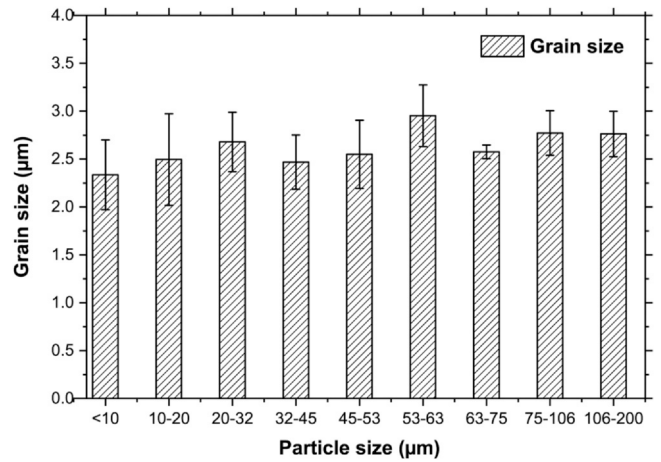
Fig. 19. Grain size average values for the studied ranges.

Table 4
Coefficient for exponential fitting and the resulting R^2 obtained.

| Miller's indexes	α	β	R^2
[111]	0.169	0.006	0.9097
[200]	0.2738	0.008	0.9629
[220]	0.3816	0.010	0.9774

onto Ti-rich areas (see Fig. 8). As an example, Fig. 14(a, c) show indentations in the middle of the Ti segregation area reporting higher values (5.07 GPa and 5.04 GPa).

The results obtained in the nano-hardness matrix were divided into colors following their exact locations in Fig. 8. The aim was to evaluate the differences between indentations in the intragranular area or matrix (orange), Ti segregation areas (violet), and mixed areas (green), as shown in Fig. 15. The effect of Ti segregation is evident, obtaining an average nanohardness value of 4.16 ± 0.14 GPa in the Ti-free intragranular areas and an average nanohardness value of 4.81 ± 0.16 GPa in Ti segregation zones.

4.3. The cooling rate of powders during solidification assessment

Several pictures of the powders in cross-section at higher magnification were investigated to assess the Secondary Dendrite Arm Spacing (SDAS), Fig. 16. A linear relationship was found between the average particle size and the SDAS.

The measured SDAS values were used to calculate the cooling rate of the particles during the atomization process. Eq. (1) was used to perform the calculation. The same formula was also used in other published work. The results obtained are in accordance with the
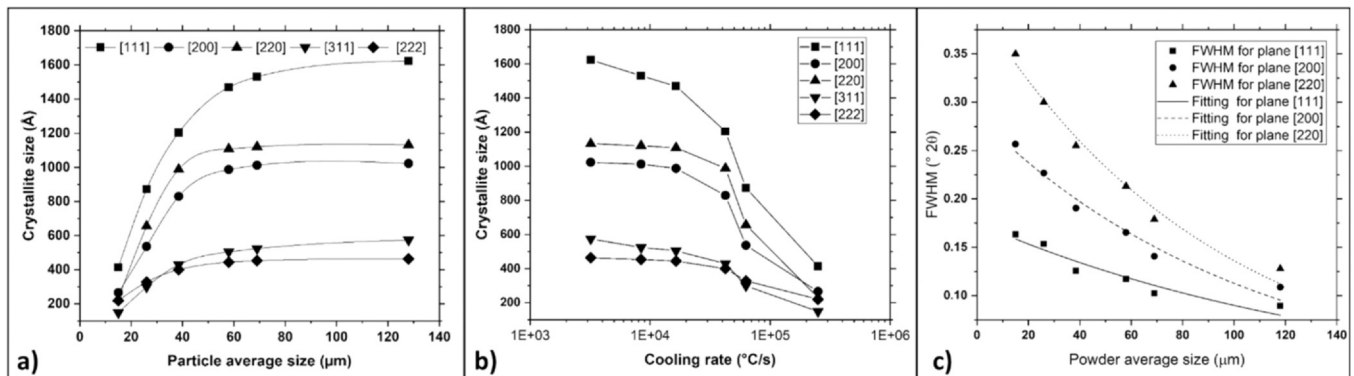
Fig. 18. Plots of the crystallite size obtained using the Scherrer equation as a function of the particle size (a) and cooling rate (b). Finally, the trend of the FWHT as a function of the particle size (c).

literature data for gas atomization where Argon was used as the carrier gas [23].

$$\log R = -2.5\log\lambda_s + 4.5 \tag{1}$$

Where R is the powder cooling rate measured in °C/s and λ_s is the SDAS expressed in μm.

According to Eq. (1), the powders' cooling rate ranges between $2.5\ E^5$ and $3.2\ E^3$ °C/s for the smallest and the largest particle. Moreover, following the above argumentation, the critical cooling rate below which Ti segregation may happen was identified at 4.0–$5.0\ E^4$ °C/s.

4.4. Powders assessed using XRD

XRD analysis was also used to determine if the particle size and their cooling rate may affect the powders diffractograms. First of all, despite the fraction of the Ti-rich microconstituents increases as the particle size increases, the XRD analysis shown in Fig. 17 was not sensitive enough to detect their presence. The XRD patterns show the same peaks for all the powders assessed independently from their average size. Despite this, the diffractograms were studied more in depth to evidence any relationship with the particle size.

The peaks found correspond to the following Miller's planes: [111]; [200]; [220]; [311]; [222]. These peaks are all compliant with the Astroloy γ phase according to the data retrieved in the databases of HighScore software by PANalytical, i.e., a Ni-γ phase rich in Co, Cr, and Mo. These results are interesting for several reasons: firstly, γ′ peaks were not found, indicating that this intermetallic was not formed, as also demonstrated by all the micrographs shown above. Secondly, after a more refined analysis performed with the same software, it was noticed that the first three peaks have a different Full Width at Half Maximum (FWHM). According to the literature, FWHM can be related to a material crystallite size via the Scherrer equation [24]. More specifically, the larger the FWHM, the smaller the crystallites. For this reason, the size of the powder crystallite was calculated, and the results are shown in Fig. 18(a). The crystallite size was calculated using all the recorded peaks, and the plot shows that they increase as the powders become coarser with an asymptotic trend. A different behavior was identified by plotting the crystallite size as a function of the cooling rate see Fig. 18(b). Naturally, as the cooling rate increases, the crystallite size became smaller, but in this case, all the curves show a flex when the cooling rate ranges between 4.2 and $6.3\ E^4$ °C/s. This specific cooling rate interval belongs to the powders with a size ranging between 45 and 52 μm, that is, those particles where Ti segregations start to be appreciable. According to this experimental experience, segregations in the interdendritic regions may affect the final crystallite size. Finally, the FWHM was plotted as a function of the particle average diameter, and an inversely proportional relationship was evidenced. As the powders became larger, the FWHM is progressively lower towards an asymptotic value. This specific trend was found for planes [111], [200], and [220], as shown below in Fig. 18(c).

An exponential fitting (see Eq. 2) was used to treat the three data sets shown in Fig. 19(c); the coefficients and the obtained R^2 values are reported in Table 4.

$$y = \alpha e^{-\beta x} \tag{2}$$

Thanks to this latter equation it is possible to correlate the FWHM to the powder size using the XRD peaks obtained from diffraction of planes with [111], [200] and [220] miller indexes.

Unlike crystallites, the grain size was similar in all particle sub-batches, even though the cooling rate is slower in the bigger particles, easing the grain growth in these types of particles. Fig. 19 gathers the average values obtained for every sub-batch studied in this work, where the average grain size is around 2.5–3 μm in all the sub-batches. Thus, it can be concluded that there is no relationship between grain size and particle size. In addition, this can corroborate that the relationship between hardness and particle size was related to the Ti segregation in coarse powder particles rather than other phenomena such as grain size.

5. Conclusions

In this paper, a batch of Astroloy powders designed for HIPping purposes was sieved and divided into several classes depending on their size. Thus, it was possible to understand the effects of each powder class on the final densified component. This research aimed to find the most balanced way to sieve powders to reduce the presence of PPBs and remove the presence of chemical inhomogeneities without excessively limiting the IGA yield.

By analyzing all the sub-batches individually, the following main conclusions can be drawn.

1. Particle flowability will be strongly enhanced by removing the 10–63 μm sub-batch. However, this choice will also affect the tap density of the particles, which could be detrimental to achieve full densification during HIP. Therefore, a strong impact on the IGA yield is forecasted as well.
2. Particles smaller than 20 μm, due to their higher specific surface, are more prone to be oxidized. Therefore, the use of these particles should be discouraged because they raise the average oxygen content in the final powder batch.
3. The surface of the smallest particles here assessed contained an Al-rich oxide layer responsible for forming PPBs in the final compact with a detrimental effect on component ductility. This effect was diffusely discussed in the literature and it will be elucidated for Astroloy in our next work.
4. A linear relationship between particle size and hardness was evidenced, meaning that the largest particles will also have higher yield stress and a different creep behavior during HIP. This irregularity should be considered when the heat treatment is designed in terms of pressure, temperature, and time. Furthermore, it was checked that this hardness increase is due to Ti segregation, which is much more intense in larger particles.
5. The grain size was discarded as a parameter that can affect the hardness in gas-atomized Astroloy powder.
6. The onset of segregation in the interdendritic regions of the larger particles is due to their lower cooling rate during solidification. This effect was particularly evident for Titanium. These chemical inhomogeneities could be eliminated by sieving away the larger particles, but this would dramatically reduce the IGA yield. This side effect can probably be mitigated or eliminated by optimizing the HIP treatment, as discussed in future work.
7. XRD diffractograms cannot directly detect the Ti segregations. Still, their FWHMs are sensitive to this aspect. Furthermore, FWHMs were influenced by the particle size and showed an exponential relationship between the FWHMs and the average particle size.
8. Sieving out the particles with a diameter smaller than 20 and larger than 110 μm will eliminate the most oxidized particles and those containing the largest segregations at the interdendritic regions

Declaration of Competing Interest

The authors declare that they have no known competing financial interests or personal relationships that could have appeared to influence the work reported in this paper.

Acknowledgements

References

[1] S. Irukuvarghula, H. Hassanin, C. Cayron, M. Aristizabal, M.M. Attallah, M. Preuss, Effect of powder characteristics and oxygen content on modifications to the microstructural topology during hot isostatic pressing of an austenitic steel, Acta Mater. 172 (2019) 6–17, https://doi.org/10.1016/j.actamat.2019.03.038

[2] G. Raisson, J.Y. Guédou, D. Guichard, J.M. Rongvaux, Production of net-shape static parts by direct HIPing of nickel base superalloy prealloyed powders, Adv. Mater. Res. 278 (2011) 277–282, https://doi.org/10.4028/www.scientific.net/AMR.278.277

[3] G. Raisson, Evolution of PM nickel base superalloy processes and products, Powder Metall. 51 (2008) 10–13, https://doi.org/10.1179/174329008×286631

[4] C.G. Hjorth, HIP powder metal near-net shapes for demanding environment and applications, J. Iron Steel Res. Int. 14 (2007) 121–125, https://doi.org/10.1016/S1006-706X(08)60064-3

[5] E. Bassini, G. Marchese, G. Cattano, M. Lombardi, S. Biamino, D. Ugues, G. Vallillo, B. Picqué, Influence of solutioning on microstructure and hardness of hot isostatically pressed Astroloy, J. Alloy. Compd. 723 (2017) 1082–1090, https://doi.org/10.1016/j.jallcom.2017.06.332

[6] E. Bassini, G. Cattano, G. Marchese, S. Biamino, D. Ugues, M. Lombardi, G. Vallillo, B. Picqu, Study of the effects of aging treatment on astroloy processed via hot isostatic pressing, Materials 12 (2019) 17, https://doi.org/10.3390/ma12091517

[7] E. Bassini, V. Vola, M. Lorusso, R. Ghisleni, M. Lombardi, S. Biamino, D. Ugues, G. Vallillo, B. Picqué, Net shape HIPping of Ni-superalloy_ study of the interface between the capsule and the alloy, Mater. Sci. Eng. A 695 (2017) 55–65, https://doi.org/10.1016/j.msea.2017.04.016

[8] J. Radavich, D. Furrer, Assessment of Russian P/M superalloy EP741NP, Superalloys 2004, TMS, 2004, pp. 381–390.

[9] J. Xie, S. Tian, X. Zhou, X. Yu, W. Wang, Influence of heat treatment regimes on microstructure and creep properties of FGH95 nickel base superalloy, Mater. Sci. Eng. A 538 (2012) 306–314, https://doi.org/10.1016/j.msea.2012.01.049

[10] C. Cai, B. Song, P. Xue, Q. Wei, J.M. Wu, W. Li, Y. Shi, Effect of hot isostatic pressing procedure on performance of Ti6Al4V: surface qualities, microstructure and mechanical properties, J. Alloy. Compd. 686 (2016) 55–63, https://doi.org/10.1016/j.jallcom.2016.05.280

[11] H.S. Liu, L. Zhang, X.B. He, X.H. Qu, H.M. Zhu, G.Q. Zhang, Effect of oxygen content and heat treatment on carbide precipitation behavior in PM Ni-base superalloys, Int. J. Miner. Metall. Mater. 19 (2012) 827–835, https://doi.org/10.1007/s12613-012-0635-x

[12] G.A. Rao, M. Srinivas, D.S. Sarma, Effect of oxygen content of powder on microstructure and mechanical properties of hot isostatically pressed superalloy Inconel 718, Mater. Sci. Eng. A 435–436 (2006) 84–99, https://doi.org/10.1016/j.msea.2006.07.053

[13] H. Shi, R. Mohanty, S. Chakravarty, R. Cabiscol, M. Morgeneyer, H. Zetzener, J.Y. Ooi, A. Kwade, S. Luding, V. Magnanimo, Effect of particle size and cohesion on powder yielding and flow, Kona Powder Part. J. 2018 (2018) 226–250, https://doi.org/10.14356/kona.2018014

[14] W.H. Qi, B.Y. Huang, M.P. Wang, Z. Li, Z.M. Yu, Generalized bond-energy model for cohesive energy of small metallic particles, Phys. Lett. Sect. A Gen Solid State Phys. 370 (2007) 494–498, https://doi.org/10.1016/j.physleta.2007.06.062

[15] M. Li, C.V.S. Lim, R. Zou, X. An, D. Wang, Multi-particle FEM modeling on hot isostatic pressing of Ti6Al4V powders, Int. J. Mech. Sci. 196 (2021) 106288, https://doi.org/10.1016/j.ijmecsci.2021.106288

[16] A. Abena, M. Aristizabal, K. Essa, Comprehensive numerical modelling of the hot isostatic pressing of Ti-6Al-4V powder: from filling to consolidation, Adv. Powder Technol. 30 (2019) 2451–2463, https://doi.org/10.1016/j.apt.2019.07.011

[17] W.C. Oliver, G.M. Pharr, An improved technique for determining hardness and elastic modulus using load and displacement sensing indentation experiments, J. Mater. Res. 7 (1992) 1564–1583 https://doi.org/doi.org/10.1557/JMR.1992.1564.

[18] C.S. Carney, R.E. Chinn, N. Doan, M.C. Gao, Isothermal decomposition kinetics of nickel (II) hydroxide powder, J. Alloy. Compd. 644 (2015) 968–974, https://doi.org/10.1016/j.jallcom.2015.03.256

[19] Q. Zhang, L. Zheng, H. Yuan, Z. Li, G. Zhang, J. Xie, Effects of composition and particle size on the surface state and degassing behavior of nickel-based superalloy powders, Appl. Surf. Sci. 556 (2021) 149793, https://doi.org/10.1016/j.apsusc.2021.149793

[20] Y.L. Kuo, K. Kakehi, Influence of powder surface contamination in the Ni-based superalloy alloy718 fabricated by selective laser melting and hot isostatic pressing, Metals 7 (2017) 367, https://doi.org/10.3390/met7090367

[21] Y.L. Kuo, K. Kakehi, Effect of the prior particle boundary on the microstructure and mechanical properties of hot-isostatic-pressed IN718 Alloy, Mater. Trans. 58 (2017) 1042–1048, https://doi.org/10.2320/matertrans.M2017045

[22] K. Opatová, I. Zetková, L. Kucerová, Relationship between the size and inner structure of particles of virgin and re-used MS1 maraging steel powder for additive manufacturing, Materials 13 (2020) 15, https://doi.org/10.3390/ma13040956

[23] P. Fang, Y. Xu, X. Li, Y. Chen, Influence of atomizing gas and cooling rate on solidification characterization of nickel-based superalloy powders, Xiyou Jinshu Cailiao Yu Gongcheng/Rare Met. Mater. Eng. 47 (2018) 423–430, https://doi.org/10.1016/s1875-5372(18)30082-1

[24] M. Kumar, S.V. Nagender Naidu, X-ray characterization of inert gas atomized low carbon astroloy powder, Mater. Sci. Eng. A 385 (2004) 1–5, https://doi.org/10.1016/j.msea.2004.02.062